University of Texas at El Paso

ScholarWorks@UTEP

2022-12-01

Fabrication And Characterization Of Iron-Based Catalysts For The Dehydrogenation Of Fossil Fuels

Victoria Isabel Reyes
University of Texas at El Paso

Recommended Citation

FABRICATION AND CHARACTERIZATION OF IRON-BASED

CATALYSTS FOR THE DEHYDROGENATION

OF FOSSIL FUELS

VICTORIA ISABEL REYES

Master's Program in Mechanical Engineering

APPROVED:

_____

Evgeny Shafirovich, Ph.D., Chair

_____

Alejandra G. Castellanos, Ph.D.

_____

Brian E. Schuster, Ph.D.

_____

Stephen L. Crites, Jr., Ph.D.
Dean of the Graduate School

DEDICATION

I would like to dedicate all the work that was put

into this thesis to my supportive parents.

FABRICATION AND CHARACTERIZATION OF IRON-BASED

CATALYSTS FOR THE DEHYDROGENATION

OF FOSSIL FUELS

by

VICTORIA ISABEL REYES, B.S.

THESIS

Presented to the Faculty of the Graduate School of

The University of Texas at El Paso

in Partial Fulfillment

of the Requirements

for the Degree of

MASTER OF SCIENCE

Department of Aerospace and Mechanical Engineering

THE UNIVERSITY OF TEXAS AT EL PASO

December 2022

ACKNOWLEDGEMENTS

ABSTRACT

For a prosperous and sustainable future, hydrogen is an encouraging solution due to its simple transition for industrial decarbonization and synergy for economic development. Paradoxically, current hydrogen production pathways release substantial amount of greenhouse gases into the atmosphere contributing to climate change. To keep up with increasing demand, hydrogen could be produced through microwave-assisted thermocatalytic dehydrogenation of fossil fuels without emitting carbon dioxide. This requires specified catalysts to meet the requirements of hydrogen yield and selectivity. The objective of the present research is to fabricate, characterize, and compare iron-based alumina ($FeAl_xO_y$) catalysts produced via solution combustion synthesis and iron-based catalysts on silicon carbide support (Fe/SiC) produced via incipient wetness impregnation. Heat mode, fuel type, and oxidizer mole ratio were varied for $FeAl_xO_y$ catalysts, and metal loading was varied for Fe/SiC catalysts. Each resultant product was characterized by X-ray diffraction analysis, scanning electron microscopy, laser diffraction particle size analysis, and Brunauer-Emmett-Teller (BET) surface area analysis. Characterization suggests that fabrication of iron-based alumina nanocomposites through solution combustion synthesis in a muffle furnace using citric acid as the fuel yields the most promising catalyst.

TABLE OF CONTENTS

LIST OF TABLES

LIST OF FIGURES

CHAPTER 1: INTRODUCTION

1.1 ENVIRONMENTALLY FRIENDLY HYDROGEN PRODUCTION

Hydrogen (H_2) is an essential element due to its multifunctional usage in the industry such as petroleum refining, ammonia production, steel manufacturing, and large-scale power generation [1]. Specifically, utilizing hydrogen as an energy carrier is a promising solution to mitigate the intrusive effects of climate change, owing to its energy security, synergy with existing industries and viable integration of renewable energy and decarbonization [2-3]. However, current hydrogen production pathways depend on fossil carbon-based energy sources and generate significant amounts of carbon emissions, 830 million tons annually [4].

To lessen the greenhouse gases' environmental impact, hydrogen production technologies are being innovated based on their feedstock availability, technology readiness level (TRL) and the amount of carbon emissions that process produces. Depending on these factors, each hydrogen production process is categorized into four "colors": grey, blue, turquoise, and green (Figure 1.1) [5]. "Grey" hydrogen is produced mainly through steam methane reforming (SMR) using natural gas, sold commercially, and is readily available. However, it is responsible for the annual emissions of 530 million tons of carbon dioxide (CO_2) emissions [4]. "Blue" hydrogen is produced through SMR with carbon capture and storage (CCS). This production process is the same as grey hydrogen, but most of the CO_2 must be captured and stored permanently, which is why it is often referred to as 'low-carbon hydrogen.' "Turquoise" hydrogen is produced through methane pyrolysis with solid carbon as a byproduct and no CO2, but it has not been used at industrial scale yet. [6] Lastly, "green" hydrogen is produced through water electrolysis that uses renewable energy to split water to hydrogen and oxygen. This process does not rely on fossil fuels and does not emit carbon dioxide [7].
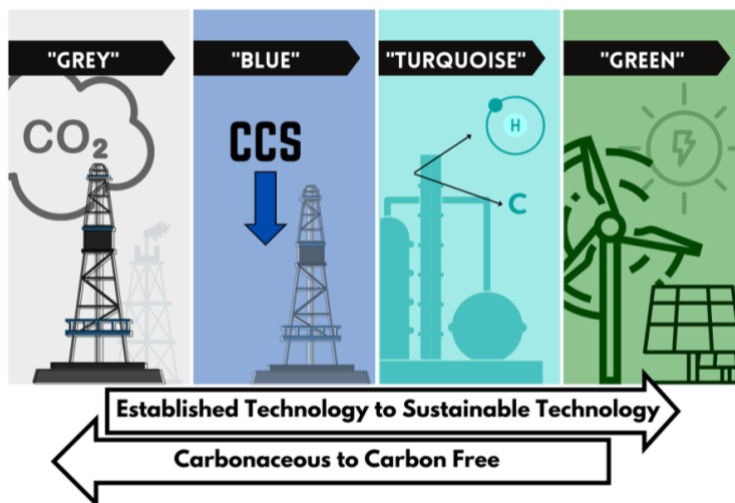
Fig. 1.1 – Depiction of four hydrogen production pathways noting differences between carbon emissions and technologies.

1.2 MICROWAVE ASSISTED DEHYDROGENATION OF FOSSIL FUELS

Since the first design of the domestic microwave oven in the 1970s, microwave chemistry has been broadly investigated for different applications. It has been shown that selective microwave heating by high-frequency radiation interacts with catalysts, intrinsically leading to less by-products and/or decomposition products. This developing technique turns hydrocarbons of natural gas and oils into high purity hydrogen ("turquoise") and solid carbon from microwave irradiation, so that carbon dioxide is not released into the atmosphere [8]. Other advantages include non-contact and rapid heating, quick start-up and shutdown, and the ability to heat the interior of the catalysts without heating the surrounding substances [9].

However, due to the complexity of this novel technology, specific catalysts must be used to meet the requirements of hydrogen selectivity, activity, and stability to retain the catalyst's structure and properties. Iron-based catalysts have been investigated due to their ability to catalytically drive the reaction and act as microwave absorbers to supply thermal energy to the system. Using iron-based catalysts supported on silicon carbide has achieved 90-98% hydrogen selectivity from methane, diesel, and gasoline with less than a fraction of CO_2 emissions. The same

2

research team also successfully achieved approximately 75-85% hydrogen selectivity from the heavier and more complex crude and extra-heavy crude oil. Despite these high hydrogen selectivity percentages, this process is far from optimized because approximately half of their theoretical yield was H_2 [10-13]. Similarly, iron-based alumina nanocomposite catalysts enabled the decomposition of plastic waste into hydrogen and solid carbon products in further research. With 76-90% hydrogen selectivity, these iron-based alumina catalysts achieved an improved hydrogen yield of 80% of the theoretical limit [11].

Often mooted with renewable energy, fossil fuels are unrivaled due to their energy density, existing widespread use and storage, and inexpensive scale production. Since they make up for 85% of the world's energy, an improved and efficient use of fossil fuels is more advantageous than complete abandonment for prosperity [14]. For example, methane dehydrogenation could be utilized since methane has the highest H/C ratio: producing significantly more energy by mass more than producing carbon dioxide and other pollutants [5,15].

1.3 RESEARCH OBJECTIVES

The objective of this research is to characterize and compare the iron-based alumina ($FeAl_xO_y$) products fabricated through solution combustion synthesis and the iron-based (Fe/SiC) products obtained through incipient wetness impregnation for their impact as catalysts for the microwave-assisted thermocatalytic dehydrogenation of fossil fuels. Furthermore, based on the characterization of the iron-based alumina nanocomposites, suggestive optimal parameters will be deduced for the solution combustion synthesis process.

CHAPTER 2: SOLUTION COMBUSTION SNTHESIS OF NANOSCALE OXIDES: LITERATURE REVIEW

Nanoparticles have been created for their numerous properties due to their small size compared to bulk material. Due to their multifunctional properties that can be tailored to a specific role, the use of nanoparticles spans across many industries from healthcare and cosmetics to environmental preservation. Among the many methods to create nanoparticles, one that was invented in the mid 1980's, is named solution combustion synthesis (SCS) [16]. This technique is highly favorable because it is a simple, rapid, and self-sustaining thermal process without usage of further thermal treatment compared to other methods. Its popularity has increased significantly in research to produce advanced materials in energy technologies, heterogenous catalysts, nanoceramics, thin films, semiconductors, and optical materials [16-17].

The system of solution combustion synthesis can be classified according to the chemical composition of the oxidizer, fuel and solvent used. Typically, metal nitrates are used as precursors and oxidizers due to their low cost, solubility in water, and relatively low decomposition temperatures. Fuels such as urea, sucrose, glycine, and citric acid provide the source of hydrogen and carbon to form complexes in metal ions that allow for homogenous mixing in the solution [19]. Altering the fuel is one of the many parameters that influences solution combustion synthesis; thus considerable properties of a good fuel entail: its solubility in the solvent used, compatibility with metal nitrates, availability, and its low decomposition temperature. Water is typically the solvent used in this reaction, but other forms such as kerosene, benzene, and several alcohols have been investigated. The oxidizers and fuels are used to calculate the stoichiometric proportion of the two for the reaction based on the reacting/oxidizing valencies of the redox (reaction-oxidation)

mixture. Furthermore, these three components of the reaction are mixed on the molecular level which allows for uniform formation of the resultant products.

This redox reaction's impetus is the system reducing its Gibbs free energy by converting chemical potential into heat. The heat required is supplied by the resulting redox after ignition. The initial reaction solution temperature is lower than the consequential combustion reaction temperature. When the temperature of the system increases, the reaction rate increases and becomes self-accelerating. When the reagents are transformed into new products, the system reaches a new equilibrium steady state [16-18].

Despite SCS's increase of popularity, there is still uncertainty of its process-structure relationship, affecting combustion parameters, due to the combustion's quick and multiphase nature. This limits the control of agglomeration and morphology of the nanoparticles fabricated, including the numerous interacting and contingent parameters of solution combustion synthesis [16, 20]. These parameters include, but not limited to the type of solution combustion technique [16], fuel type [19-21], fuel to oxidizer ratio and precursor ratio [16, 21-23], amount of solvent [24, 25], ignition temperature [16, 26], heat mode [17, 27] and solution pH [28-29]. Another drawback of solution combustion synthesis is the assumption of the stoichiometric reaction yielding nitrogen, water, and carbon dioxide. Yet, the actual process is more complex and could release nitrous oxides that are harmful to environment [16]. Further testing and thorough studying on structure formation could be developed in the future to tailor to the desired morphology of the resultant products produced through solution combustion synthesis.

CHAPTER 3: EXPERIMENTAL

3.1 SYNTHESIS

3.1.1 Solution Combustion Synthesis (SCS)

In the solution combustion synthesis of iron-based alumina nanocomposites, iron nitrate nonahydrate ($Fe(NO_3)_3 \cdot 9H_2O$) and aluminum nitrate nonahydrate ($Al(NO_3)_3 \cdot 9H_2O$) are used as the precursors and oxidizers with an organic fuel. Two organic fuels were tested in the present work: citric acid ($C_6H_8O_7$) (CA) and glycine ($C_2H_5NO_2$) (G). The reactions to yield the product with 1:1 Fe/Al mole ratio are described by the following equations:

$$Fe(NO_3)_3 \cdot 9H_2O + Al(NO_3)_3 \cdot 9H_2O + \frac{5}{6}C_6H_8O_7 \rightarrow \frac{1}{4}Fe_2O_3 + \frac{1}{4}Al_2O_3 + 5CO_2 + \frac{37}{3}H_2O + \frac{3}{2}N_2 \qquad (3.1)m$$

$$Fe(NO_3)_3 \cdot 9H_2O + Al(NO_3)_3 \cdot 9H_2O + \frac{5}{3}C_2H_5NO_2 \rightarrow \frac{1}{4}Fe_2O_3 + \frac{1}{4}Al_2O_3 + \frac{10}{3}CO_2 + \frac{79}{6}H_2O + \frac{7}{3}N_2 \qquad (3.2)$$
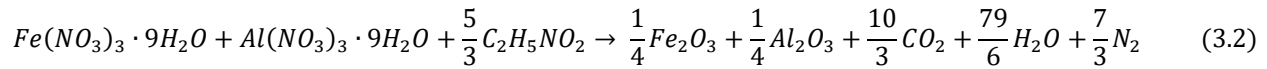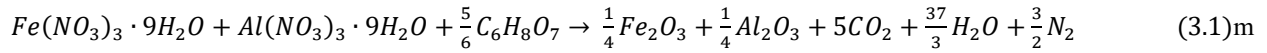
In the present work, two other Fe/Al mole ratios were also tested: 1:2 and 2:1. This was achieved by respective changes in the mole ratio of the two nitrates. Note that the amount of the fuel was changed accordingly to maintain the combustion stoichiometry. Table 3.1 shows the used amounts of the reactants and distilled water for each solution.

Table 3.1: Compositions of mixtures for solution combustion synthesis of iron-based alumina nanocomposites.

Fe:Al	$Al(NO_3)_3 \cdot 9H_2O$	H_2O	$Fe(NO_3)_3 \cdot 9H_2O$	H_2O	$C_6H_8O_7$	H_2O
	g	ml	g	ml	g	ml
1:2	2.251	3.517	1.211	1.894	1.441	2.440
1:1	1.688	2.640	1.818	2.840	1.441	2.440
2:1	1.125	1.758	2.424	3.787	1.441	2.440
Fe:Al	$Al(NO_3)_3 \cdot 9H_2O$	H_2O	$Fe(NO_3)_3 \cdot 9H_2O$	H_2O	$C_2H_5NO_2$	H_2O
	g	ml	g	ml	g	ml
1:2	2.250	3.507	1.210	1.888	1.126	4.505
1:1	1.762	2.630	1.670	2.832	1.126	4.505
2:1	1.125	1.754	2.425	3.776	1.126	4.505

Mixing was conducted using a polytetrafluoroethylene (PTFE) magnetic stir-bar. Each reactant was mixed with distilled water for 5 minutes individually, and then all of them were mixed together for 10 minutes at room temperature in a 50 ml beaker. The solution was then heated on a hotplate or in a muffle furnace (these two heating modes were compared in the present work).

3.1.2 Incipient Wetness Impregnation (IWI)

The so-called incipient wetness impregnation (IWI) is used to prepare the additional catalysts tested in this work for comparison with those obtained by SCS. Iron nitrate nonahydrate (same as the one described in Section 3.1.1) which serves as the metal precursor, is mixed for 5 minutes with distilled water according to the amounts shown in Table 3.2. Using a pipet, the aqueous solution is then squeezed onto the silicon carbide powder (SiC) (beta phase, 99% metals basis. Alfa Aesar), the support material. The product is then mixed on a hotplate at 150°C for 3 hours with a PTFE magnetic stir-bar, until the final product became a slurry/sludge. The slurry is then dried in a muffle furnace overnight at 150°C for 12 hours to expel any remaining distilled water and finally calcinated at 350°C for 3 hours. These Fe/SiC catalysts were synthesized with three different metal loadings: 5 wt%, 10 wt%, and 20 wt%.

Table 3.2: Compositions of mixtures to produce Fe/SiC catalysts through incipient wetness impregnation.

Fe	SiC	$Fe(NO_3)_3 \cdot 9H_2O$	SiC	H_2O
wt%	wt%	g	g	ml
5	95	2.5	6.585	4.0
10	90	2.5	3.118	4.0
20	80	2.5	1.385	4.0
5	95	5.0	13.17	8.0
10	90	5.0	6.238	8.0
20	80	5.0	2.772	8.0
5	95	10	26.34	16
10	90	10	12.48	16
20	80	10	5.540	16

3.2 CHARACTERIZATION

3.2.1 X-ray Diffraction (XRD)

The Bruker D8 Discover X-Ray Diffraction (XRD) instrument (Fig. 3.1) was used to identify the crystalline phases and present XRD patterns by applying Cu Kα radiation ($\lambda = 1.5406$ Å). Before measurements, the sample powders must be prepared. The powder is evenly distributed onto a slide, which is then placed securely onto a stage in the instrument (Fig. 3.2). Due to the radiation emitted, all safety doors must be locked before running the test. After setting the testing parameters on the program with a scan speed of 2.5°/min, the XRD scan was able to run for each sample tested. These measurements occur when the x-ray beam hits the periodic array of molecules in a crystal, resulting in incident ray beams that diffract in different directions that can be predicted by Bragg's Law. Once the run is complete, the data is shown as a spectrum, and the peaks that are prominent on the graph are then matched to a database using the DIFFRAC.EVA software, to identify the material.

Fig. 3.1 – Bruker D8 Discover XRD instrument.
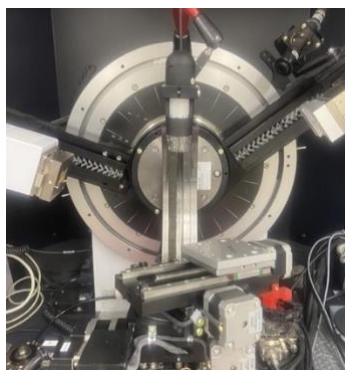
Fig. 3.2 – Experimental setup of the instrument.

3.2.2 Scanning Electron Microscopy (SEM)

The Hitachi S-4800 High-Resolution Scanning Electron Microscopy (SEM) instrument (Fig 3.3) and the Hitachi SU-3500 SEM instrument (Fig 3.4) were used to provide distinctive morphology and chemical composition of the samples produced through SCS and IWI. For

examination, each sample is stuck onto a carbon sticker. The aluminum stage used in the instruments must be covered with a copper tape before placing the carbon stickers (Fig 3.5). After setting the proper working distance and vacuum conditions, the sample can be observed in either instrument. This characterization method uses an electron beam to excite (and ultimately eject) an electron from a lower energy shell of the sample. The void left behind is then filled by an electron from a higher energy shell, and the difference in energy between the shells is released in the form of x-rays [30]. Because these x-rays are characteristic to each element, chemical composition can be determined through energy dispersive spectroscopy.

Fig. 3.3 – Hitachi S-4800 High Resolution SEM instrument.

Fig. 3.4 – Hitachi SU-3500 SEM instrument.
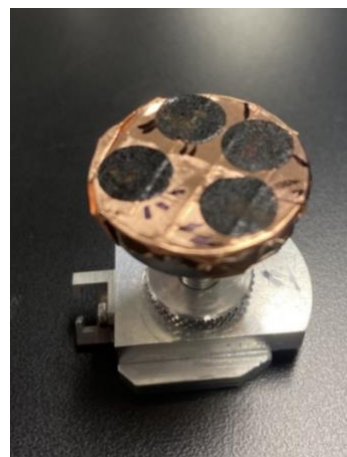
Fig. 3.5 – Samples stuck with copper tape for the stand used in the SEM.

3.2.3 Laser Diffraction Particle Size Analysis

The Microtrac Bluewave instrument (Fig. 3.6) was used to determine the particle size distribution of the resulting powders produced through solution combustion synthesis and incipient wetness impregnation. First, isopropyl alcohol or distilled water, is used to pour in the conical flask in a sample delivery controller of the instrument as the liquid carrier. After preliminary set-zero measurements, 0.5-2 grams of the sample was added until the sample loading display showed 'RUN'. This can be achieved by adding more of the sample, activating the ultrasonic probe, or

diluting the sample in the mixing chamber. When the display was ready, the measurement was calculated in less than 2 minutes through laser diffraction. This tri-laser and multidetector optical system measures the angular variation in intensity as a function of Mie's theory and Fraunhofer's diffraction when the laser beam scatters through the particulate sample.

Fig. 3.6 – Microtrac Bluewave particle size analyzer (right) with sample delivery controller (left).

3.2.4 BET Surface Area Analysis

The HORIBA SA-9600 Brunauer-Emmett-Teller (BET) Multipoint Surface Area Analyzer (Fig. 3.7) was used to determine each nanocomposite's specific surface area. Prior to sample measurements, the helium and nitrogen tanks, seen in Figure 3.7, must be verified it is secure and connected to their respective inlet in the instrument. Once the valves on each tank are opened, the flow control valve must be set to 40 ± 5 psi pressure on the helium's and nitrogen's respective regulators. Afterwards, each powder can now be measured to be transferred inside the sample cell (Fig. 3.8) using the PTFE funnel (Fig. 3.9). A minimum of 0.5 grams of the sample produced through incipient wetness impregnation is required for the BET to determine the surface area. Approximately 0.1 grams of the sample produced through solution combustion synthesis is required for the BET measurement. Each sample cell is then inserted into their adapters at prep stations #1 and #2. The two samples are then degassed using heating sleeves at 300°C for 2 hours to remove moisture and other contaminants.

After the sample is degassed, one sample cell is transferred to the analysis port of the instrument, where a Dewar flask is also filled, according to safety operating procedures and equipment, with liquid nitrogen and placed onto the inactive moving bed (Fig. 3.10). After inserting the required measurements of the sample into the SA-9600 software, the analysis can now be initiated. During the analysis, the Dewar flask is raised submerging the sample and then lowers to compute adsorption and desorption values three times. The sample is submerged in liquid nitrogen so that the temperature can be maintained. This allows the nitrogen's molecules to be adsorbed on the surface of the sample creating a monolayer of nitrogen molecules, to determine the surface area based on the size of molecules of nitrogen and the molecules adsorbed by the surface. Since the volume of the sample cell needs to be calibrated before and after each measurement, helium gas is used for a 'blank' run since helium doesn't adsorb onto the sample.

Fig. 3.7 – HORIBA SA 9600 BET Multipoint Surface Area Analyzer with secured helium and nitrogen tanks.

Fig. 3.8 – Empty sample cell where sample powder is placed inside.

Fig. 3.9 – PTFE funnel.
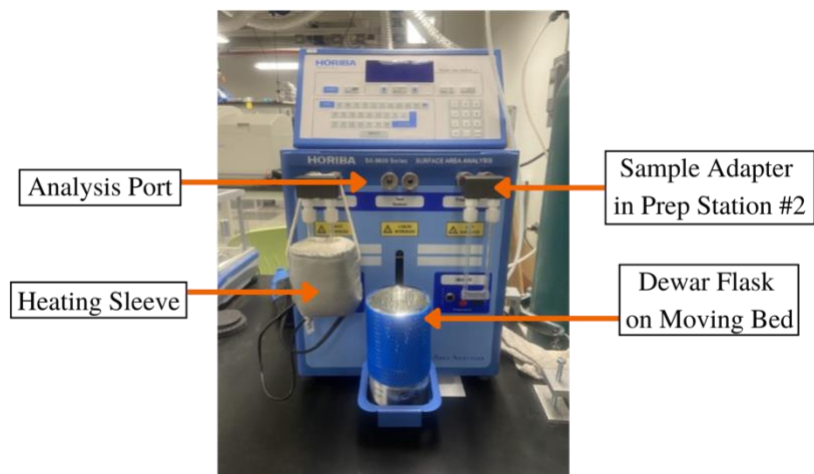
Fig. 3.10 – HORIBA SA-9600 BET Multipoint SAA with accessories.

CHAPTER 4: RESULTS AND DISCUSSION

4.1 SOLUTION COMBUSTION SYNTHESIS

4.1.1 Combustion Behavior

During the solution combustion synthesis of any citric acid experiments on the hotplate, it was first observed that thick and large bubbles were formed due to boiling, with water droplets on the sides of the beaker. Afterwards, the mixture released grey fumes with no visible flames with a decrease of volume from the initial solution. Finally, the brown and black solid products were formed and left to cool before proper disposal procedures (Fig 4.1a-d). Each experimentation lapsed for approximately 20 minutes from start to cool-down, while the duration of the combustion reaction was approximately 15-30 seconds. The same behavior was seen for all three experiments that varied the Fe/Al mole ratios (1:2, 1:1, 2:1).
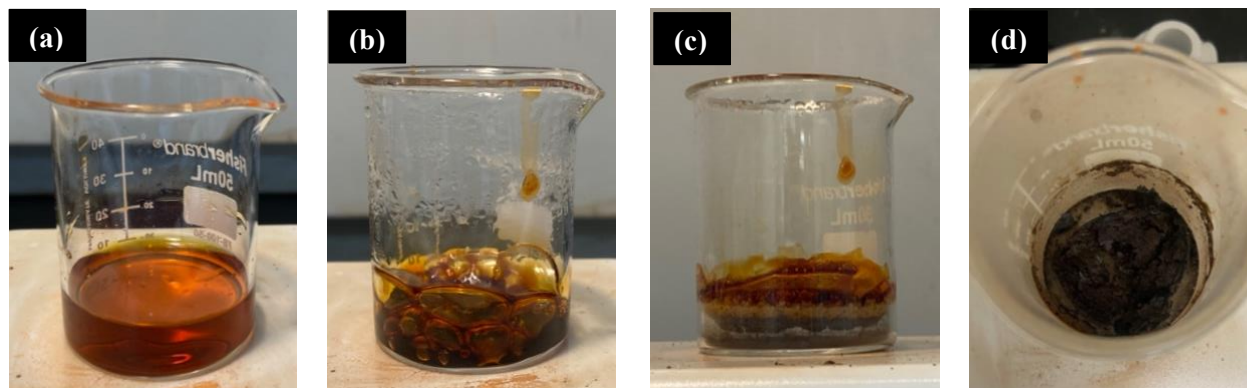
Fig. 4.1 – Combustion behavior of the mixture with citric acid as a fuel: (a) initial solution, (b) bubbles forming, (c) combustion, (d) final product.

During the solution combustion synthesis of any glycine experiments, it was first observed that smaller bubbles rose accompanied with water evaporation on the sides of the beaker. However, each of the three Fe/Al mole ratios exhibited its own combustion behavior. The 1:2 Fe/Al experiments mimicked the behavior of the SCS experiments using citric acid with grey fumes, as the combustion traveled up the beaker without any visible flames (Fig 4.2). In contrast, the

experiments with 1:1 and 2:1 ratio exhibited an incandescent flame during combustion, including long fibrous products erupting from the beaker which can be seen in Figures 4.3-4.4. The 2:1 ratio SCS experiment compared to the 1:1 had a much brighter flame and resulted in a darker mixture of orange and black products. Lastly, since the SCS experiments are done in an enclosed muffle furnace, it is assumed that the same behavior can be expected as the SCS experiments of glycine in the hotplate, but the final products had a darker and homogeneous color. There was also less of an eruption of fibrous products, which mostly remained inside the beaker.
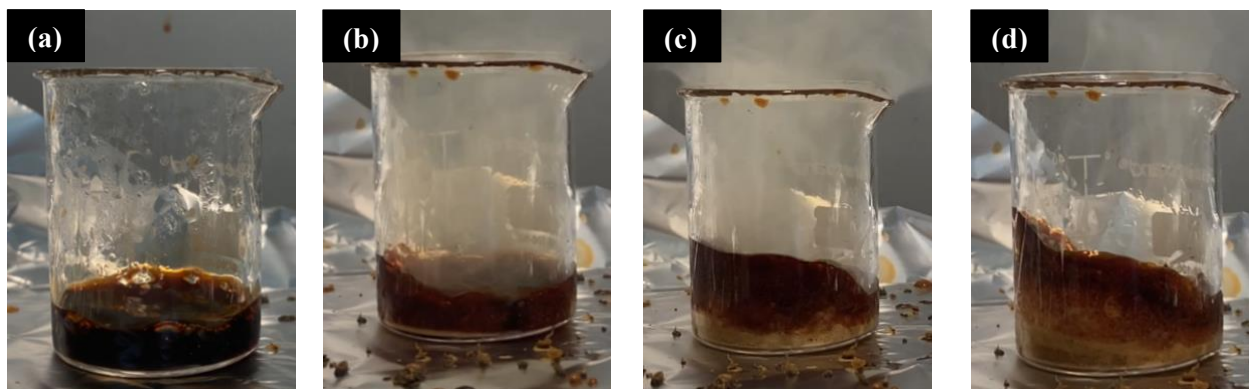
Fig. 4.2 – Combustion behavior of 1:2 Fe/Al, glycine-based SCS on a hotplate: (a) initial bubbles, (b) fumes observed, (c) products visually seen from the bottom of the beaker, (d) after combustion.
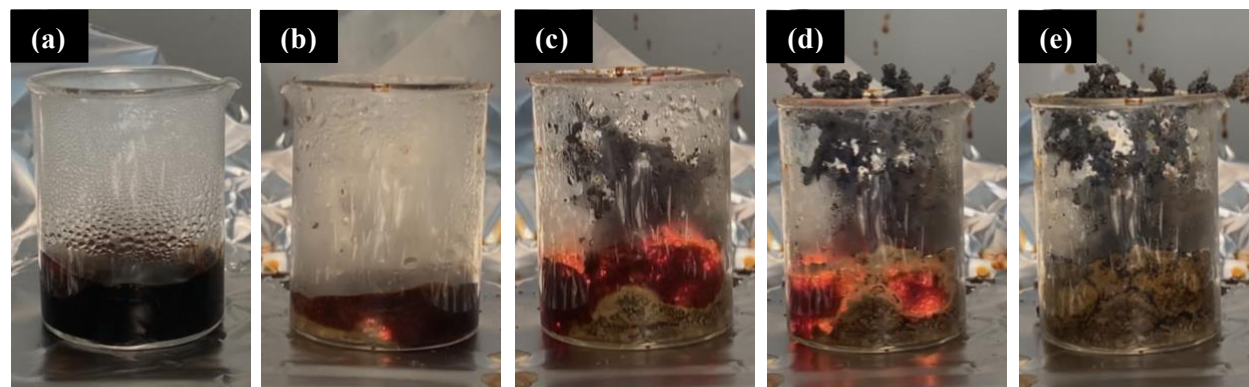
Fig. 4.3 – Combustion behavior of 1:1 Fe/Al, glycine-based SCS on a hotplate: (a) initial solution, (b) first visible flame, (c) fibrous products erupting, (d) products escaping beaker, (e) after combustion.
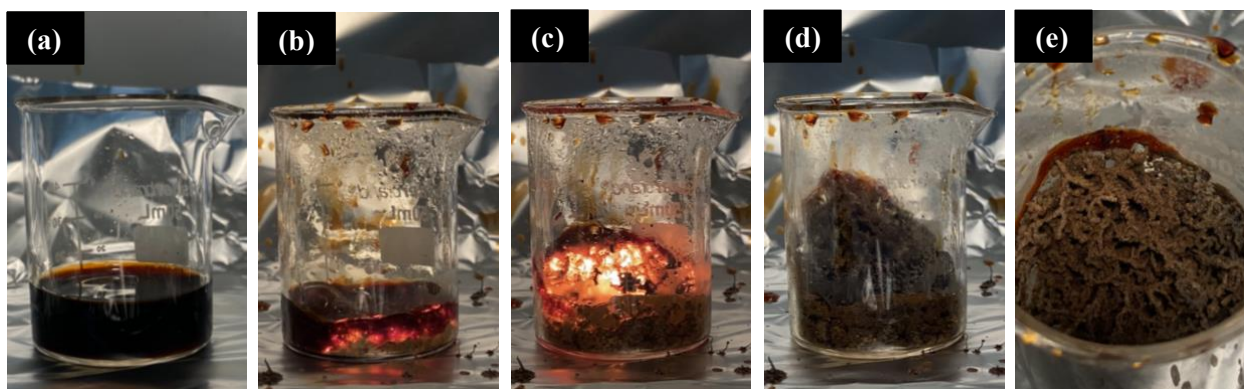
Fig. 4.4 – Combustion behavior of 2:1 Fe/Al, glycine-based SCS on a hotplate: (a) initial solution, (b) initial combustion, (c) bright flame observed, (d) end of combustion, (e) final products.

Through observation, SCS products produced in a furnace, regardless of fuel type, resulted in a more homogenous color than those produced on a hotplate due to the uniform heat transfer in a muffle furnace. For all the products, the increase of iron affected the final color from lightest to darkest (left to right in Figures 4.5-4.8) because of the different iron oxides forming during combustion. Relative to the fuel type, SCS experiments conducted with citric acid resulted in a darker color (brown and black) than those that were performed with glycine (orange and grey). In Figure 4.7, the left side of the image shows the fibrous products that erupted from the beaker while the right side shows the final products ground using an agate mortar and pestle. To conclude, all products visually were affected by the varied fuel type, Fe/Al ratios, and heat mode.

Fig. 4.5 – IBA products through SCS using citric acid on a hotplate: (a) 1:2 Fe/Al ratio, (b) 1:1 Fe/Al ratio, (c) 2:1 Fe/Al ratio.

Fig. 4.6 – IBA products through SCS using citric acid in a furnace: (a) 1:2 Fe/Al ratio, (b) 1:1 Fe/Al ratio, (c) 2:1 Fe/Al ratio.

Fig. 4.7 – IBA products through SCS using glycine on a hotplate: (a) 1:2 Fe/Al ratio, (b) 1:1 Fe/Al ratio, (c) 2:1 Fe/Al ratio.

Fig. 4.8 – IBA products through SCS using glycine in a furnace: (a) 1:2 Fe/Al ratio, (b) 1:1 Fe/Al ratio, (c) 2:1 Fe/Al ratio.

4.1.2 X-ray Diffraction (XRD)

XRD patterns were obtained for all the products produced through solution combustion synthesis with the varied parameters. Figure 4.9 shows the amorphous structure of the SCS products with a 1:2 (Fe/Al) mole ratio between the citric acid and glycine – independent of heat mode. Figures 4.10 and 4.11 show the crystalline structure of the SCS products with 1:1 Fe/Al and 1:2 Fe/Al mole ratios for citric acid and glycine – dependent of heat mode. Characteristic peaks were identified in Figures 4.10 and 4.11 as follows:

1) 1:1-CA-H: 30.78º, 36.65º, 43.69º, 54.89º, 58.37º and 64.24º.
2) 1:1-CA-F: 30.61º, 35.61º, 43.48º, 54.44º, 58.17º, 63.78º and 75.22º.
3) 2:1-CA-H: 30.51º, 36.43º, 43.39º, 57.61º and 63.17º.
4) 2:1-CA-F: 30.57º, 35.84º, 43.56º, 57.72º and 63.19º.
5) 1:1-G-H: 30.78º, 36.31º, 44.00º, 44.50º, 54.70º, 55.28º, 58.33º, 58.97º, 64.11º, 64.85º, 73.00º, 76.01º, 76.90º and 89.32º.
6) 1:1-G-F: 30.89º, 36.38º, 44.45º, 55.35º, 58.98º and 64.86º.
7) 2:1-G-H: 30.66º, 36.13º, 43.97º, 54.56º, 58.22º, 63.99º, 72.55º and 74.81º.
8) 2:1-G-F: 30.88º, 36.33º, 44.32º, 55.13º, 58.72º and 64.36º.
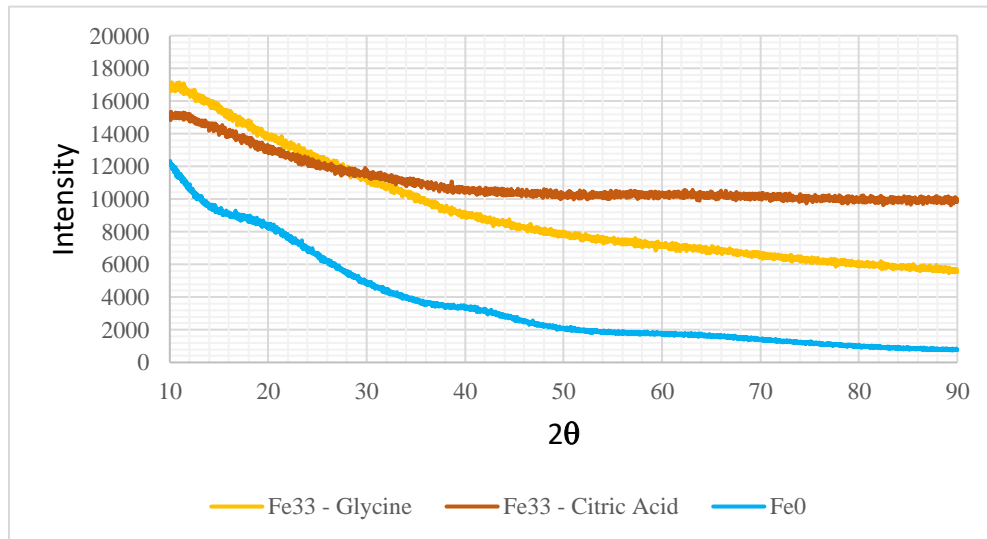
Fig. 4.9 – XRD Patterns of SCS products with 1:2 Fe/Al mole ratios.
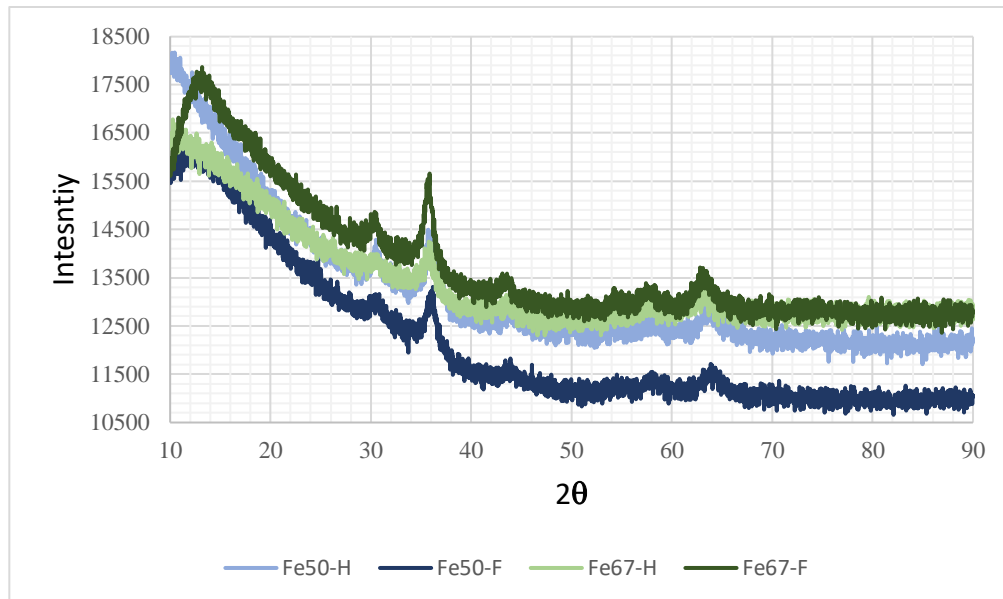
Fig. 4.10 – XRD patterns of citric acid-based SCS products with 1:1 Fe/Al and 2:1 Fe/Al mole ratios.
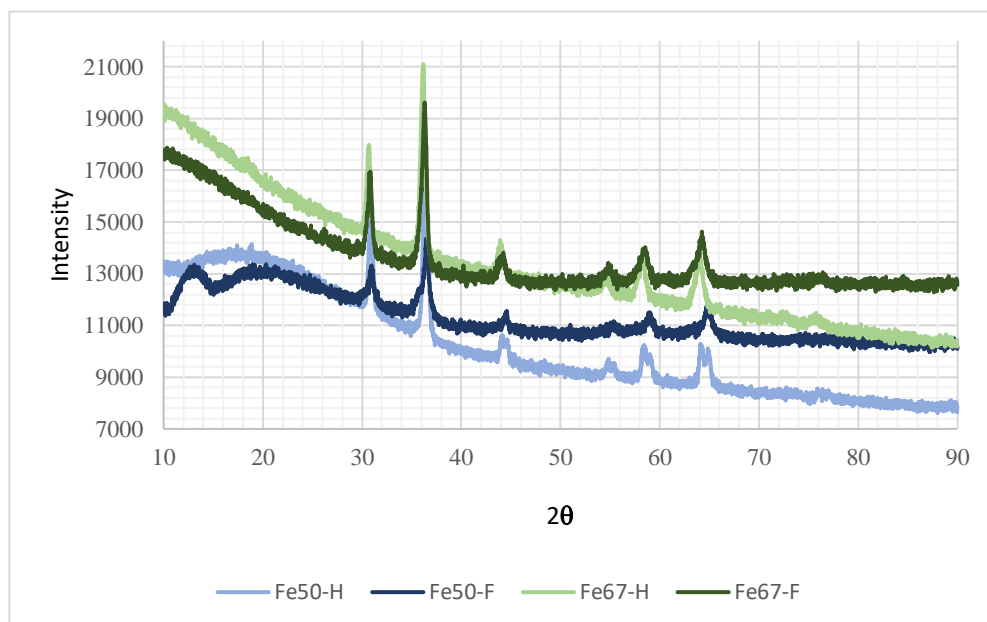
Fig. 4.11 – XRD patterns of glycine-based SCS products with 1:1 Fe/Al and 2:1 Fe/Al mole ratios.

According to Figure 4.9, the iron-lean products had an amorphous structure as well as the

0:1 Fe/Al mole ratio of citric acid compared (light blue). This is distinctive trait of the highly

amorphous Al_2O_3 which is forming due to the high aluminum-rich mole ratios. The 1:1 citric acid-

based products in both heat modes were difficult to identify due to its low crystallization which

can be seen in Figure 4.12. The DIFFRAC.EVA software best matched the products to aluminum

18

iron oxide ($AlFe_2O_4$) and hercynite ($FeAl_2O_4$). Figure 4.12c-d show the more crystalline glycine-based SCS products in the furnace and hotplate, respectively. The XRD spectrum in Figure 4.12c was best matched to magnetite (Fe_3O_4) and hercynite. The characteristic peaks in Figure 4.12d are similar to those in Figure 4.12c and were best matched to two phases of hercynite. Fuel type, heat mode and the Fe/Al mole ratio all heavily influenced the XRD spectrum.
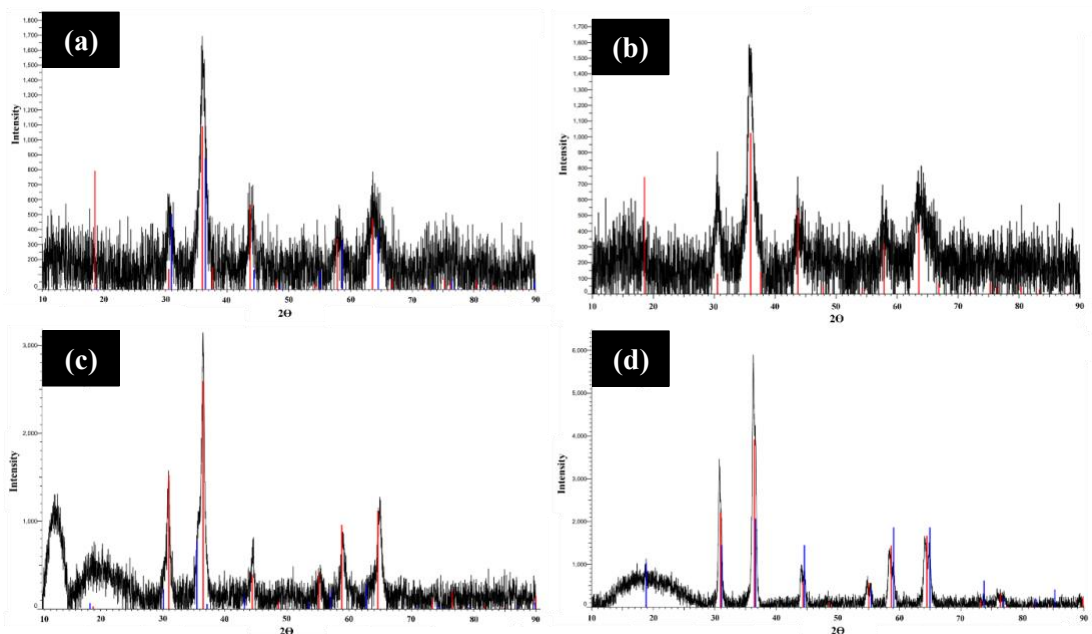
Fig. 4.12 – XRD patterns of S.C.S products with 1:1 Fe/Al mole ratio: (a) CA in a furnace, (b) CA on a hotplate, (c) G in a muffle furnace, (d) G on a hotplate.

4.1.3 Scanning Electron Microscopy (SEM)

The surface morphology of the iron-based alumina catalysts was observed with the Hitachi S-4800 SEM instrument using secondary electrons for imaging. Figures 4.13 and 4.14 present the images of the SCS products that used citric acid as the fuel, while Figures 4.15 and 4.16 present the images of the SCS products that used glycine as a fuel. All these images ranged from x180k to x60 magnification. It is apparent that in comparison of the two fuels, the glycine SCS products, regardless of heat mode and Fe/Al ratio, had a different topography than those with citric acid. The glycine SCS products had multiple pores that ranged from < 100 nm to about 15 µm, while citric

19

acid SCS products had a flaky appearance. There are also images that display over-sintering of particles due to agglomeration in Figure 4.3.1.
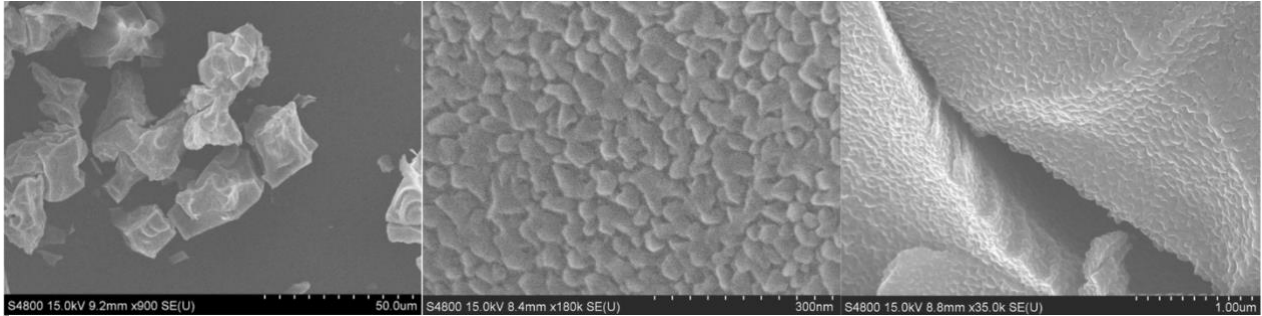
Fig. 4.13 – SEM images of S.C.S products with CA on a hotplate: (a) 1:2 Fe/Al ratio, (b) 1:1 Fe/Al ratio, (c) 2:1 Fe/Al ratio.
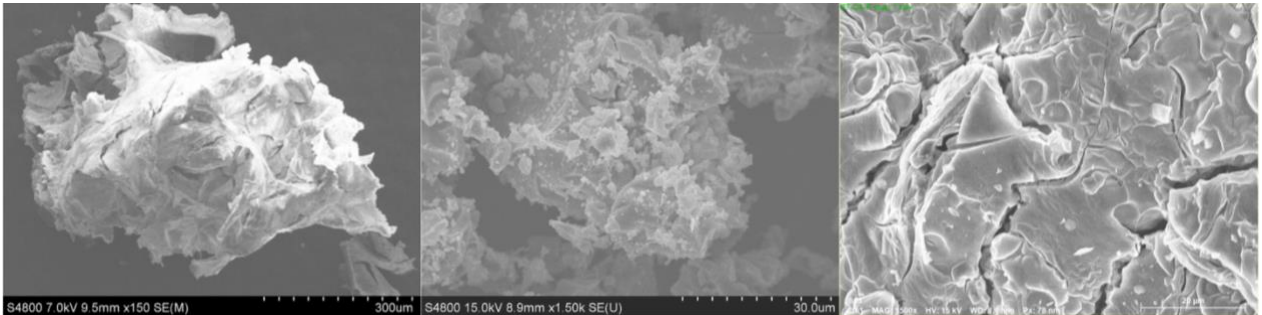
Fig. 4.14 – SEM images of S.C.S products with CA in a muffle furnace: (a) 1:2 Fe/Al ratio, (b) 1:1 Fe/Al ratio, (c) 2:1 Fe/Al ratio.
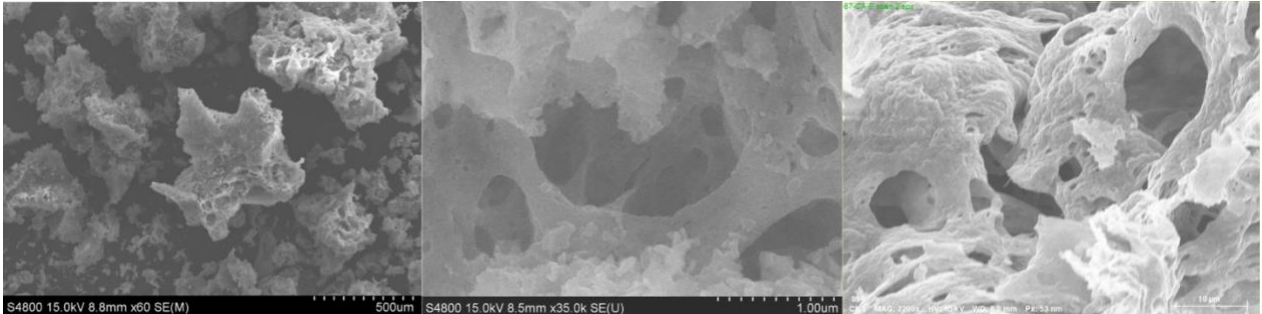
Fig. 4.15 – SEM images of S.C.S products with G on a hotplate: (a) 1:2 Fe/Al ratio, (b) 1:1 Fe/Al ratio, (c) 2:1 Fe/Al ratio.
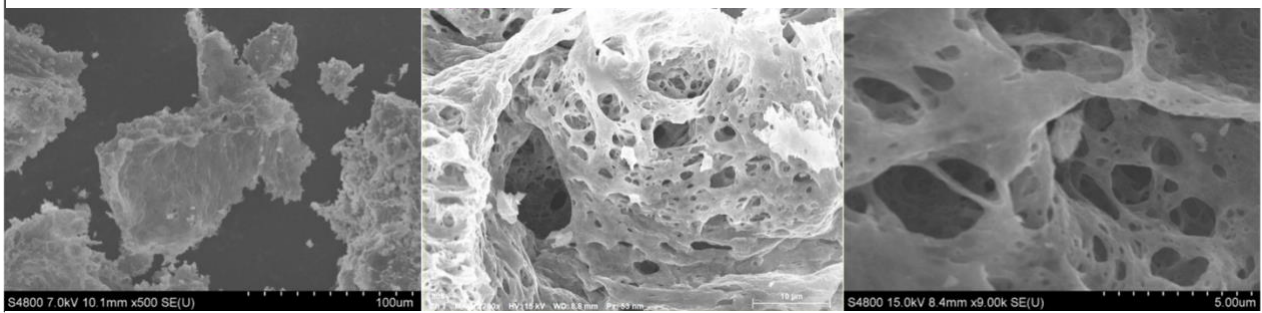
Fig. 4.16 – SEM images of S.C.S products with G in a muffle furnace: (a) 1:2 Fe/Al ratio, (b) 1:1 Fe/Al ratio, (c) 2:1 Fe/Al ratio.

The morphology of the nanoparticles captured in Figures 4.13 – 4.16 shows that the nanoparticles are more dependent on the fuel type used in solution combustion synthesis than the effects caused by heat mode and Fe/Al mole ratio. The porous structure of the glycine SCS products was a result of the volatile flame that was previously mentioned in the combustion behavior of glycine products. In further examination according to Figure 4.17, pure aluminum oxide (0:1 Fe/Al mole ratio) exhibited smoother surfaces in comparison to Figure 4.18. Figure 4.18 represents pure iron oxide (1:0 Fe/Al mole ratio), which exhibits the same rough and flaky surfaces seen in Figure 4.14 of SCS products produced with citric acid. This suggests that iron embeds onto the alumina support such as the iron embedding onto the silicon carbide support in incipient wetness impregnation.
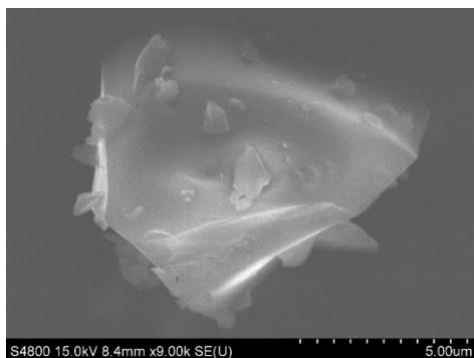
Fig. 4.17 – SEM image of pure aluminum oxide. (0:1 Fe/Al mole ratio).
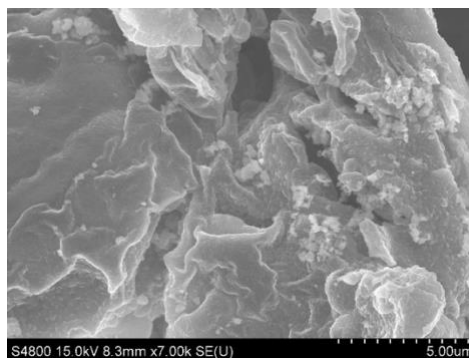
Fig. 4.18 – SEM image of pure iron oxide. (1:0 Fe/Al mole ratio).

4.1.4 Laser Diffraction Particle Size Analysis

Figures 4.19 and 4.20 show the particle size distributions of the powders obtained by solution combustion synthesis with the two fuels, two heat modes, and three Fe/Al mole ratios tested. The mean volume diameters of the SCS products are shown in Table 4.1. The mole ratio did not affect the mean volume diameter and median diameter.
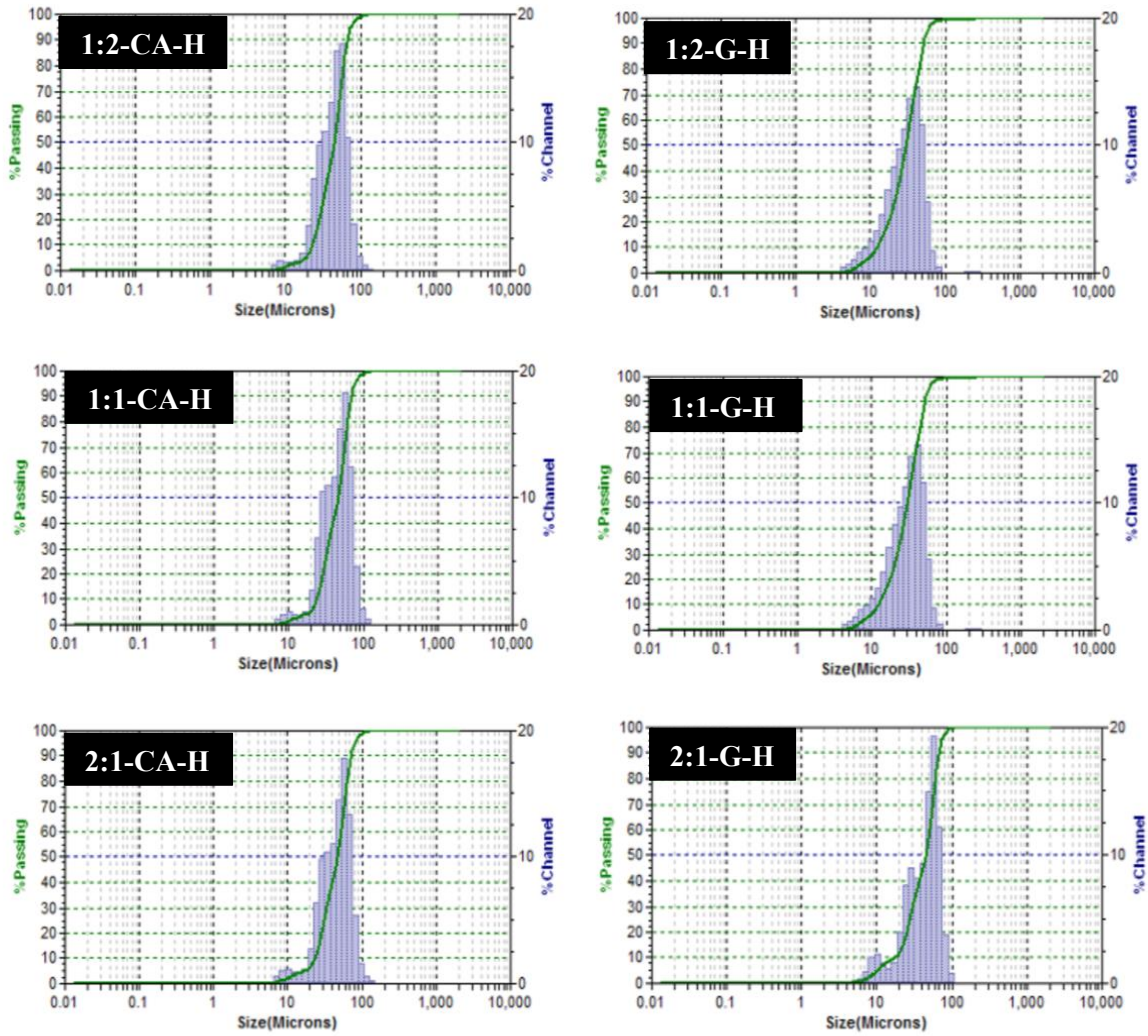
Fig. 4.19 –Particle size distributions of the powders obtained in SCS experiments that used (left) citric acid or (right) glycine as the fuel on a hotplate with 3 Fe/Al ratios in ascending order from top to bottom.
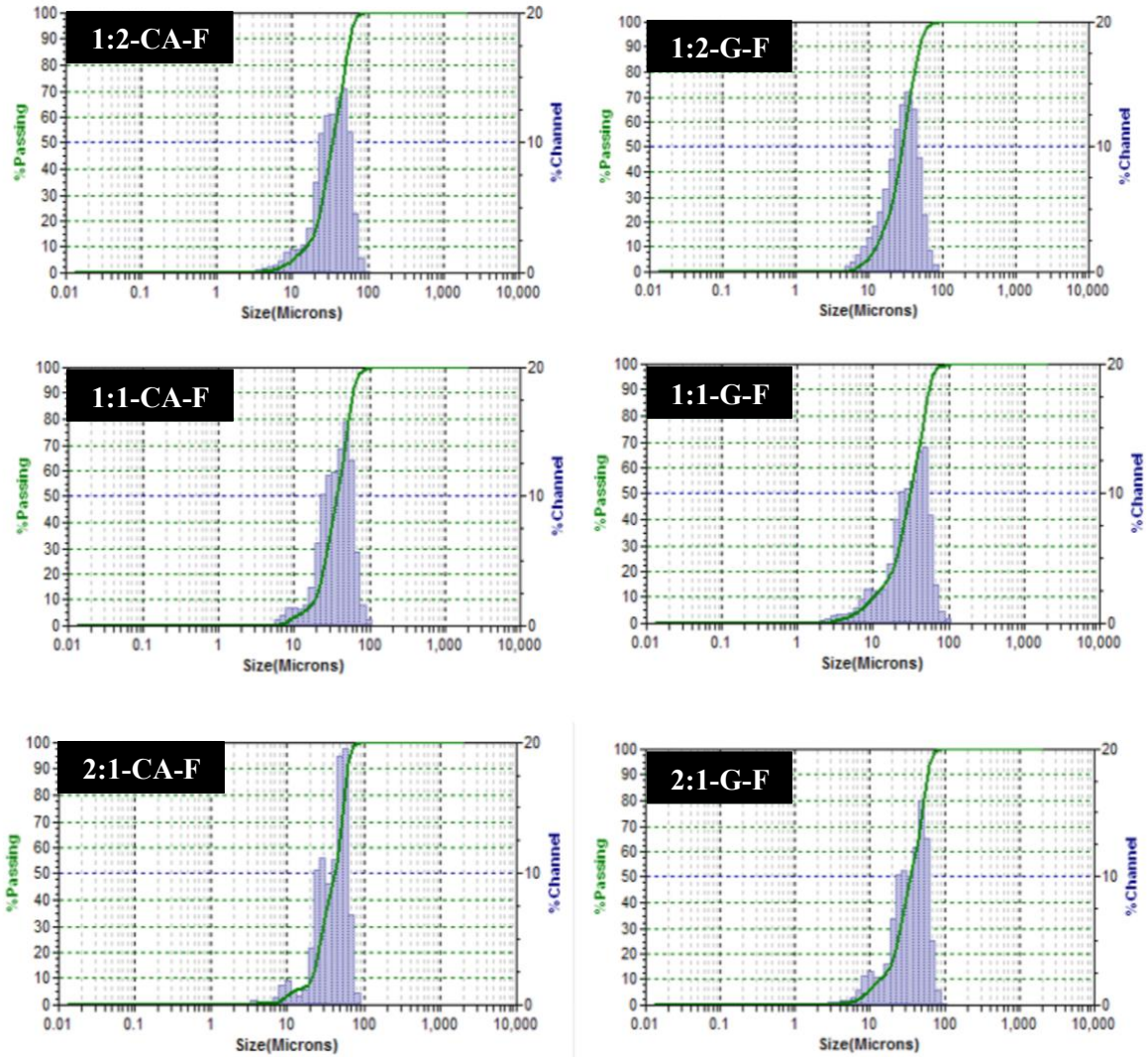
Fig. 4.20 –Particle size distributions of the powders obtained in SCS experiments that used (left) citric acid or (right) glycine as the fuel in a muffle furnace with 3 Fe/Al ratios in ascending order from top to bottom.

Table 4.1 – Mean Volume Diameter of SCS Products.

Fuel	Fe/Al mole ratio	Heat Mode	Mean Volume Diameter (μm)	Standard Deviation (μm)
Citric Acid	1:2	Hotplate	43.33	2.31
	1:2	Furnace	37.09	1.04
	1:1	Hotplate	41.48	2.77
	1:1	Furnace	39.28	2.80
	2:1	Hotplate	40.33	4.96
	2:1	Furnace	40.20	2.01
Glycine	1:2	Hotplate	28.28	2.52
	1:2	Furnace	33.12	4.51
	1:1	Hotplate	33.75	3.48
	1:1	Furnace	32.72	5.61
	2:1	Hotplate	42.10	1.94
	2:1	Furnace	34.34	4.08

The citric acid solutions yielded particles with a narrower particle size distribution relative to the glycine products. The narrower the particle size distribution, the more product is produced in that specified size range, which contributes to high specific surface areas – better for catalysis. Yet, it is still noted that the mean particle size measured for citric acid-based experiments was approximately 5.0 μm more than in the glycine-based experiments, which can be seen in Table 4.4. There was not a significant effect of the other two parameters: heat mode, and Fe/Al mole ratios, on the particle size distribution.

4.1.5 BET Surface Area Analysis

Figures 4.21 and 4.22 present the average values of the iron-based alumina nanocomposites that were produced by solution combustion at various parameters. Figure 4.21 shows the

measurements that used citric acid as a fuel, while Figure 4.22 presents the measurements that

used glycine as a fuel; all graphs differentiate the three Fe/Al ratios used as well. Table 4.2 presents

the values shown in Figures 4.21 and 4.22.

Table 4.2 – Specific Surface Areas of SCS Products

Fuel	Fe/Al mole ratio	Heat Mode	Iteration 1 ($\frac{m^2}{g}$)	Iteration 2 ($\frac{m^2}{g}$)	Iteration 3 ($\frac{m^2}{g}$)	Mean ($\frac{m^2}{g}$)
Citric Acid	1:2	Hotplate	215.6	101.3	108.9	141.9
	1:2	Furnace	108.7	250.7	276.2	211.9
	1:1	Hotplate	149.5	138.9	183.4	157.3
	1:1	Furnace	196.2	194.6	199.4	196.7
	2:1	Hotplate	89.91	141.4	95.55	108.9
	2:1	Furnace	104.5	121.8	118.5	114.9
Glycine	1:2	Hotplate	37.92	41.27	38.89	39.36
	1:2	Furnace	35.59	42.90	55.13	44.54
	1:1	Hotplate	10.79	12.84	14.52	12.72
	1:1	Furnace	50.65	29.07	48.58	42.77
	2:1	Hotplate	3.11	2.83	4.11	3.35
	2:1	Furnace	12.60	10.23	11.90	11.58
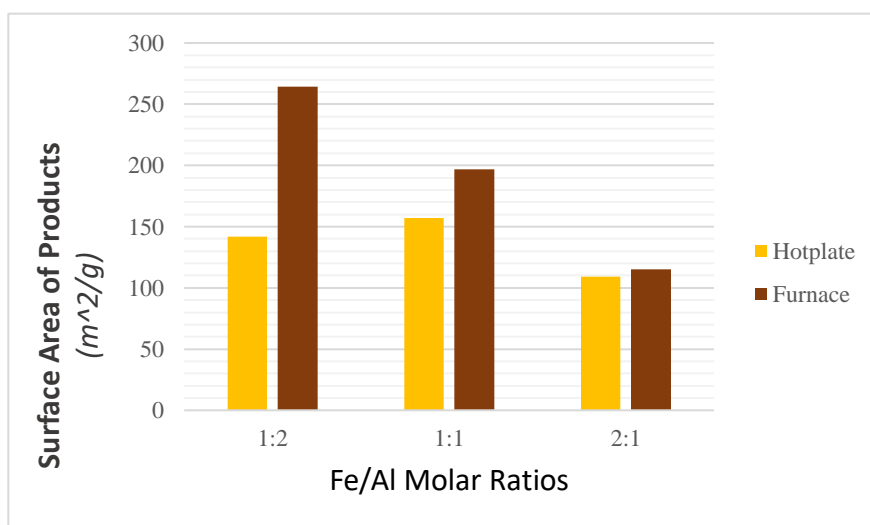
Fig. 4.21 – Mean specific surface areas of iron-based alumina catalysts produced through SCS with CA at varied parameters.
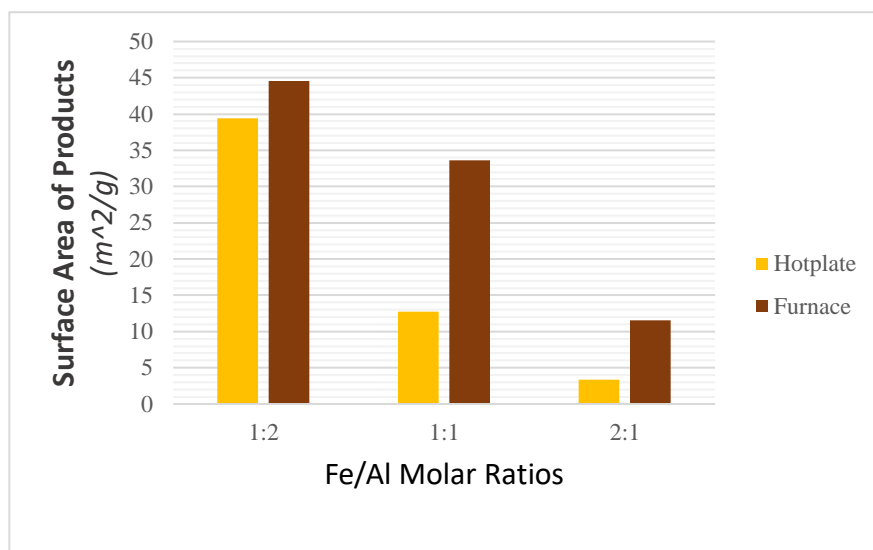
Fig. 4.22 – Mean specific surface areas of iron-based alumina catalysts produced through SCS with G at varied parameters.

The specific surface area was strongly dependent on the (1) heat mode, (2) fuel type, and (3) Fe/Al mole ratio. First, the SCS iron-based alumina products created in a muffle furnace had a higher specific surface area than those obtained on a hotplate. Secondly, citric acid products had a higher specific surface area, approximately $164.1 \frac{m^2}{g}$, compared to glycine products, approximately $24 \frac{m^2}{g}$, which is close to previously reported values in literature. Lastly, within the three oxidizer ratios from 1:2 Fe/Al to 2:1 Fe/Al, iron-lean mixtures produced higher specific surface area. The highest specific surface area measured in SCS experiments using citric acid was $276.2 \frac{m^2}{g}$ (using a furnace and 1:2 Fe/Al mole ratio). The highest specific surface area measured in SCS experiments using glycine was $55.13 \frac{m^2}{g}$ (using a furnace and 1:2 Fe/Al mole ratio). Another notable parameter that affected the surface area was the duration of mixing of the aqueous solution prior to combustion. Longer stir times generated large specific surface areas.

4.2 INCIPIENT WETNESS IMPREGNATION

4.2.1 Process Characteristics

During the mixing of the metal precursor, distilled water, and support material on the hotplate with a magnetic stir-bar, bubbles were seen on the beaker as the water evaporated (Fig. 4.23a). After thorough mixing, the aqueous solution turned into a grey sludge, which can be seen in Figure 4.23b. The sludge is then placed into a muffle furnace for drying and calcination.
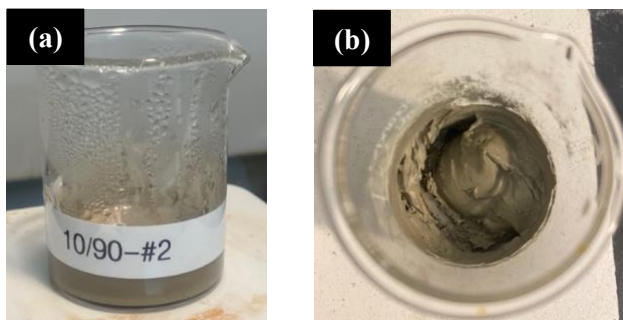
Fig. 4.23 – Process characteristics of incipient wetness impregnation: (a) evaporation seen during 10 wt.% Fe loading, (b) grey sludge observed after mixing.

Figure 4.24 displays the final products of the Fe/SiC catalysts produced through incipient wetness impregnation with a distinct color change as the iron metal loading increased from 5 wt% to 20 wt%, which was also seen in the solution combustion products. For catalyst fabrication, incipient wetness impregnation is a much longer process than solution combustion synthesis, which happens in seconds. However, incipient wetness impregnation is technically simpler with less amount of waste. It was also noted that the increase of iron weight loading resulted in less amount of final Fe/SiC products.
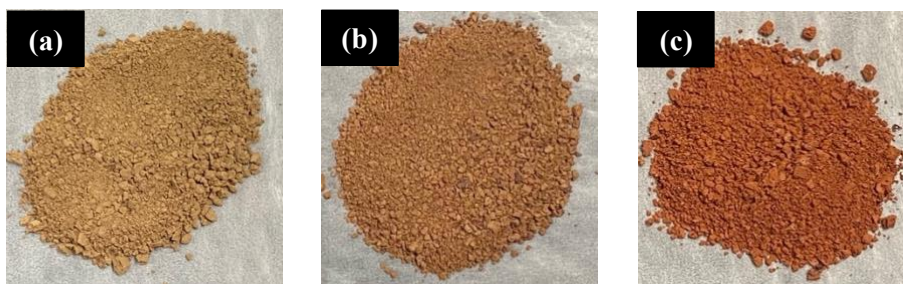
Fig. 4.24 – Fe/SiC catalysts produced through incipient wetness impregnation:
(a) 5 wt% Fe, (b) 10 wt% Fe, (c) 20 wt% Fe.

4.2.2 X-ray Diffraction (XRD)

Figure 4.25 shows XRD patterns of the products that had a metal loading of 5 wt%, 10 wt%, and 20 wt%. The characteristic peaks were observed at 24.26°, 33.15°, 35.64°, 41.25°, 49.48°, 62.41°, 63.77°, 71.85° and 71.67° for 20 wt% Fe, and at 35.56°, 41.42°, 60.01°, 71.76°, 75.82° and 89.99° for SiC for all three metal loadings of 5 wt%, 10 wt% and 20 wt%. DIFFRAC.EVA software also matched the peaks to Fe_2O_3, which is an iron oxide phase named Hematite (blue peaks) and $\beta - SiC$, which is a silicon carbide phase called Moissanite (red peaks) independent of metal loading.
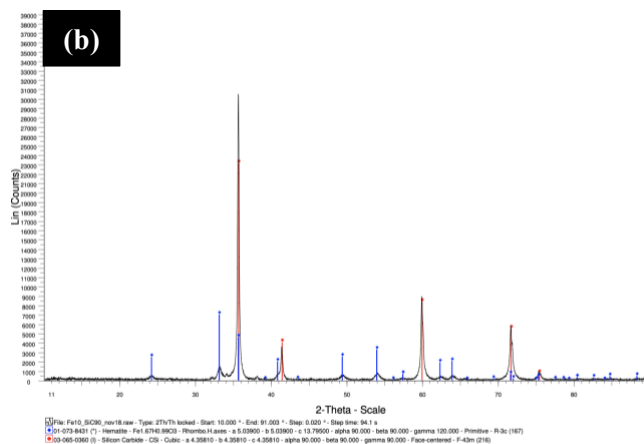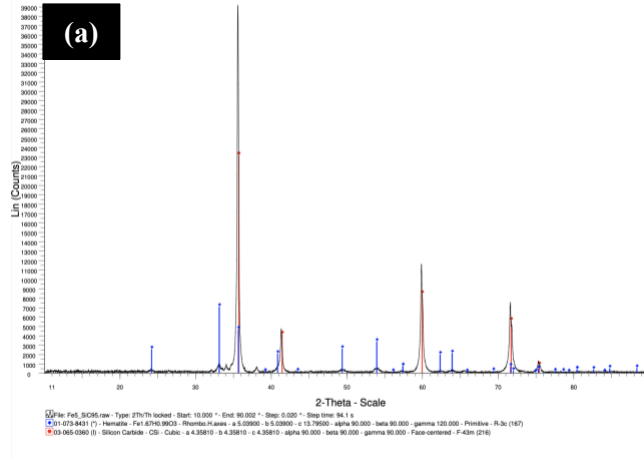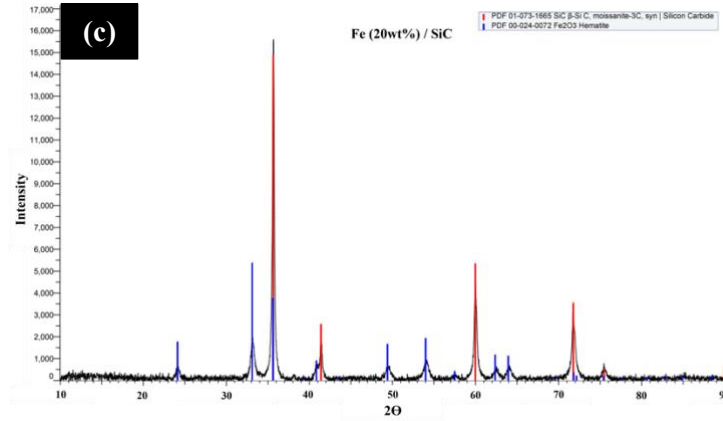
Fig. 4.25 – XRD Spectra of Fe/SiC catalysts produced through incipient wetness impregnation: (a) 5 wt% Fe, (b) 10 wt% Fe, (c) 20 wt% Fe.

According to Figure 4.26, the crystalline structure of each Fe/SiC catalyst did not change except for the heightened peaks that are relative to silicon carbide since their loading changes from 80 wt% to 95 wt%. This was expected according to the literature.
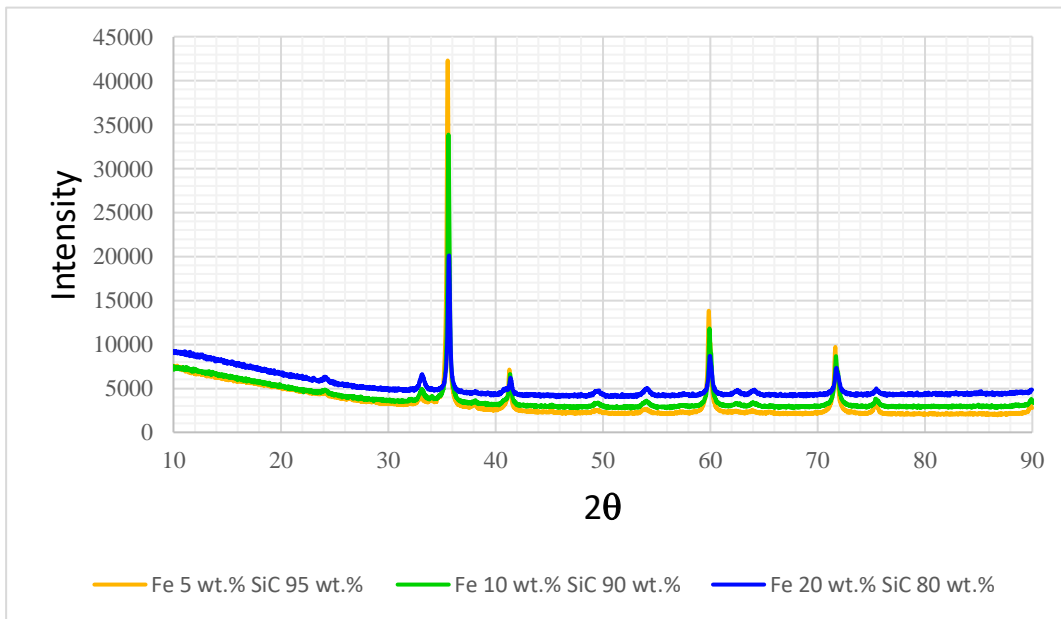
Fig. 4.26 - XRD patterns of the incipient wetness impregnation products.

4.2.3 Scanning Electron Microscopy (SEM)

The surface morphology of the Fe/SiC catalysts was observed with the Hitachi SU-3500 SEM instrument using back-scattered electrons to increase elemental contrast. Large samples, 100 – 400 microns, were used due to agglomeration. Figures 4.27 – 4.32 show the obtained SEM images and EDS spectra. The SEM images in Figures 4.27, 4.29, and 4.31 reveal that the Fe/SiC catalysts are not porous materials unlike the products produced through solution combustion synthesis using glycine as a fuel. Each image showed similar topography despite different metal loadings. It is also confirmed by using energy dispersive spectroscopy (EDS) that the atomic weight loadings of the iron nitrate and silicon carbide quantitatively match the Fe/Si atomic ratios at 5 wt% Fe, 10 wt% Fe, and 20 wt% Fe when removing carbon and oxygen out of the spectra in Figures 4.28, 4.30 and 4.32.
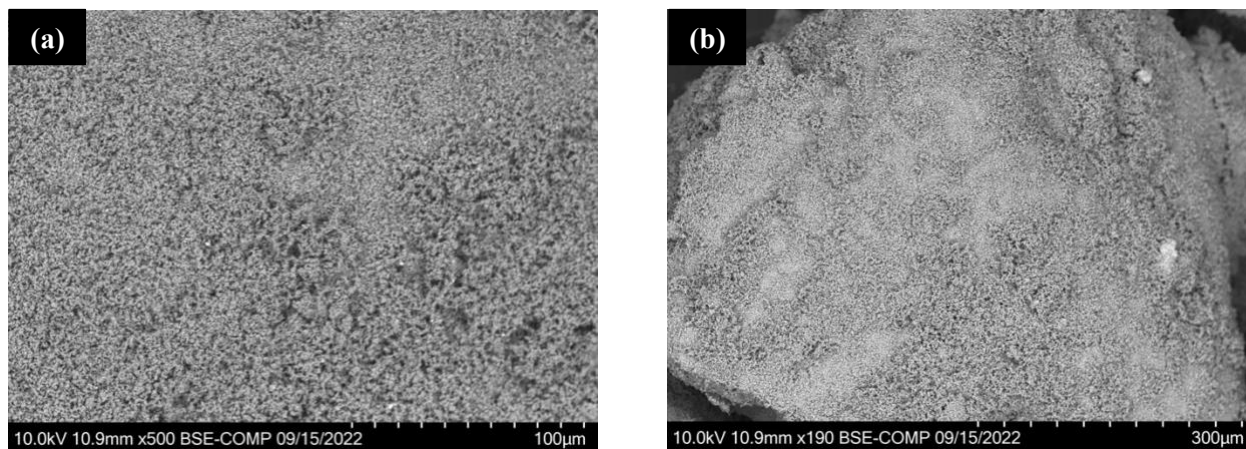
Fig. 4.27 – SEM images of Fe/Si catalyst, 5 wt% Fe: (a) x500 magnification (b) x190 magnification
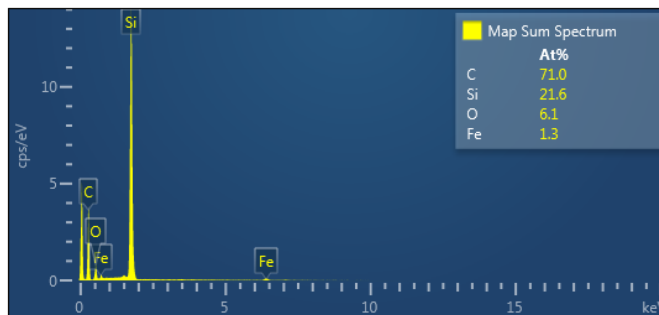
Fig. 4.28 – EDS spectra of Fe/Si catalyst, 5 wt% Fe.
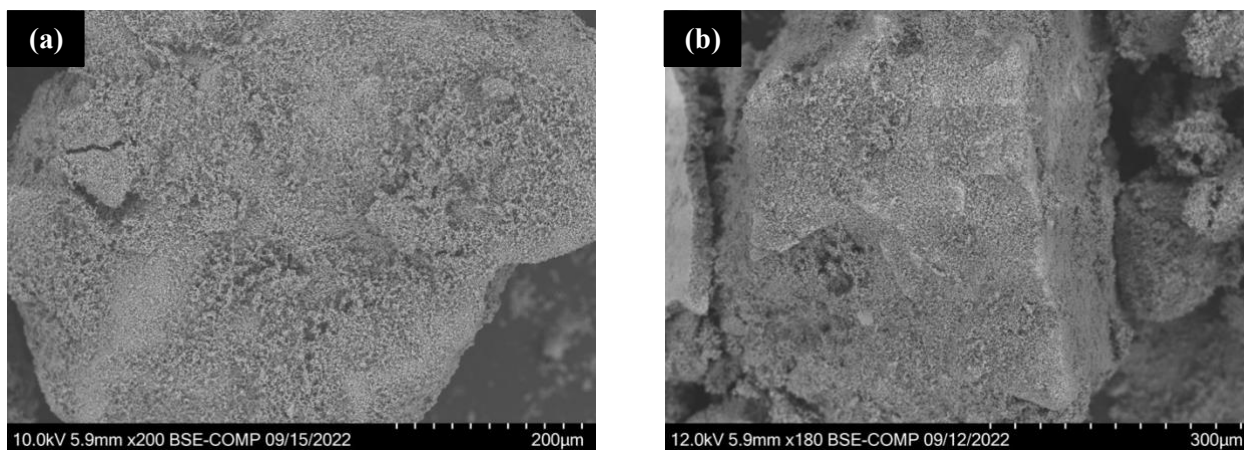
Fig. 4.29 – SEM images of Fe/Si catalyst, 10 wt% Fe: (a) x200 magnification (b) x180 magnification.
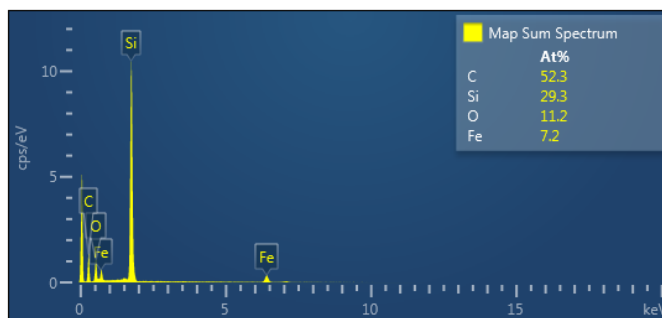
Fig. 4.30 – EDS spectra of Fe/Si catalyst, 10 wt% Fe.
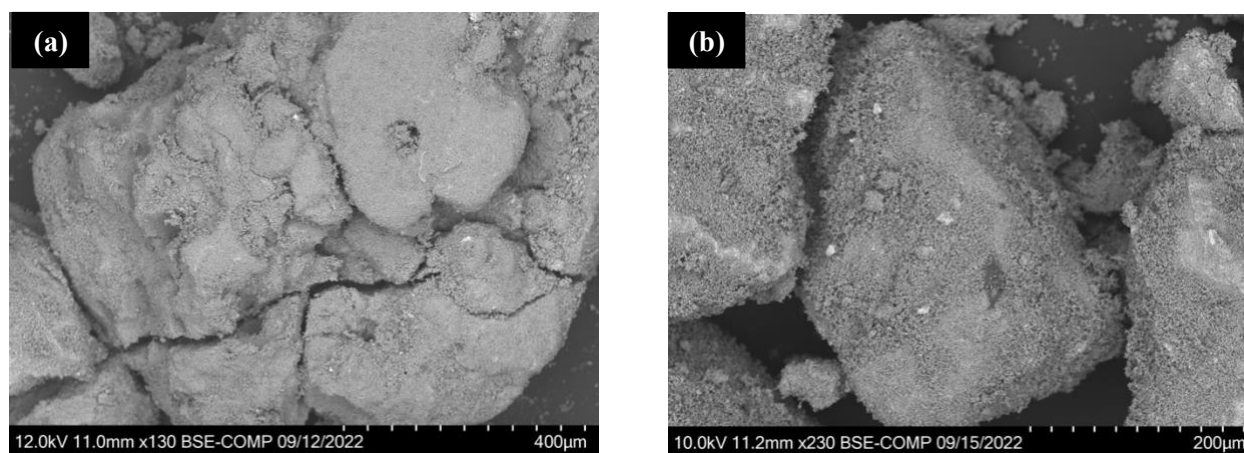
Fig. 4.31 – SEM images of Fe/Si catalyst, 20 wt% Fe: (a) x230 magnification (b) x130 magnification.
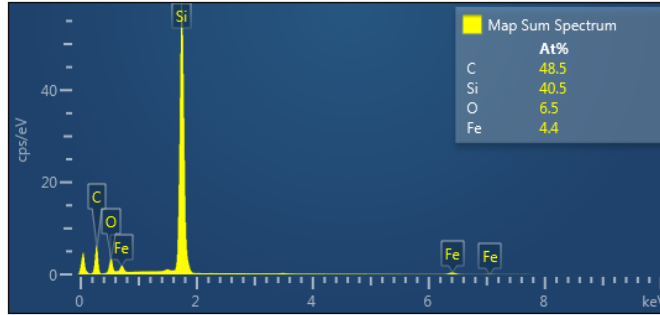
Fig. 4.32 – EDS spectra of Fe/Si catalyst, 20 wt% Fe.

Visually, each particle had a rough surface in an irregular shape before and after tumbling. Using energy dispersive spectroscopy (EDS), it was shown that SiC particles are the larger particles with the smaller (20 – 100 nm) Fe particulates covering each particle. The number of Fe particulates increased as the Fe loading increased from 5 wt% to 20 wt%.

4.2.4 Laser Diffraction Particle Size Analysis

Figure 4.33 shows the particle size distributions of the samples produced through incipient wetness impregnation with different metal loadings. A bimodal particle size distribution was observed for each sample. The mean volume diameter and the median diameter varied from 196.1 to 293.5 μm.
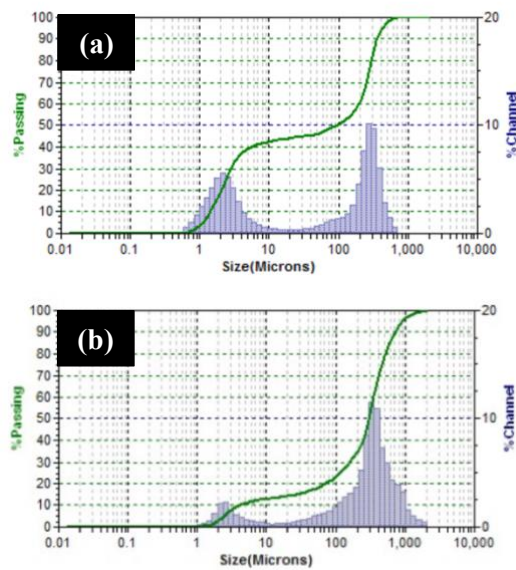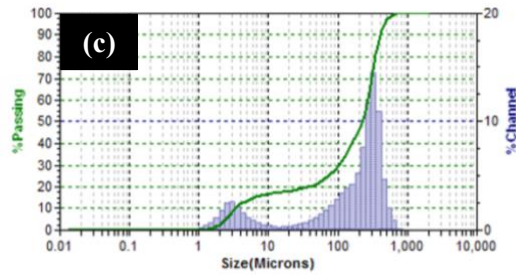
Fig. 4.33 – The particle size distributions of the IWI products: (a) 5 wt% Fe,
(b) 10 wt% Fe, (c) 20 wt% Fe.

The particle size distributions shown in Figure 4.33 dramatically changed after mixing the samples in the Bioengineering Inversina Tumbler Mixer for 2-5 minutes. This was to rule out bubble peaks that happen when distilled water is used as the liquid carrier. Figure 4.34 shows that the resulting particle size distribution has a single peak and a mean volume diameter of 9.11 µm. The overall range is from 3.12 µm to 13.9 µm.
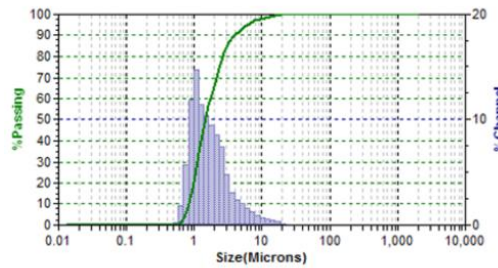
Fig. 4.34 – Particle size distribution of products produced through
incipient wetness impregnation at 5 wt% Fe after tumbling.

4.2.5 BET Surface Area Analysis

Table 4.3 and Figure 4.35 show the determined specific surface areas. Each sample was replicated three times to confirm validity of the values, which is why the bar graph represents average values.

Table 4.3 –Specific surfaces areas of IWI products.

Fe wt%	Mean Specific Surface Area ($\frac{m^2}{g}$)	Standard Deviation ($\frac{m^2}{g}$)
5	13.5	1.1
10	14.4	0.8
20	17.9	1.3
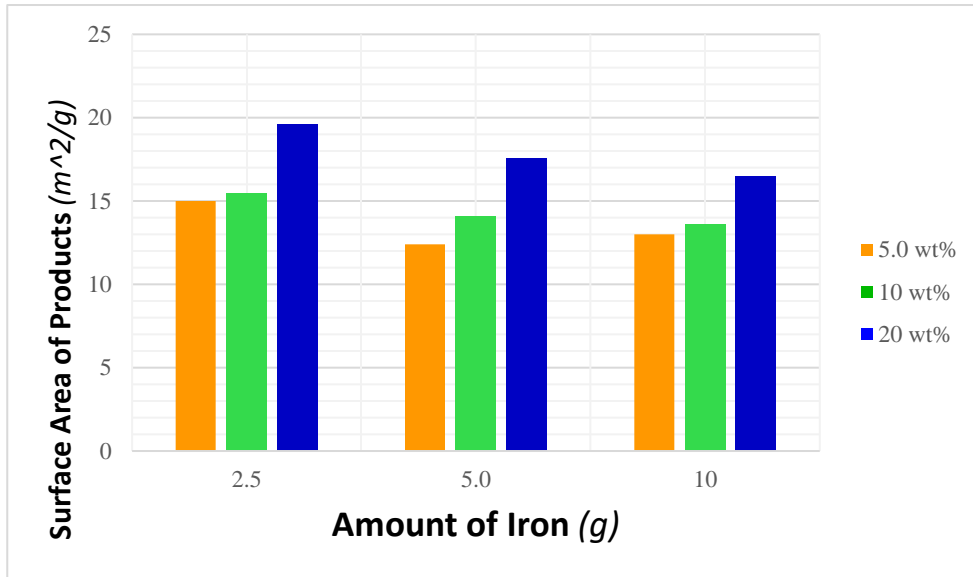
Fig. 4.35 – Mean specific surface areas of Fe/SiC catalysts at different Fe weight loadings.

The average specific surface area for the products produced through incipient wetness impregnation was approximately 15.24 $\frac{m^2}{g}$, which is why products produced through solution combustion synthesis are superior regarding the high surface area needed for catalysis. However, the specific surface area increased from 13.48 $\frac{m^2}{g}$ to 17.87 $\frac{m^2}{g}$ as the metal loading increased from 5 wt% to 20 wt%. Yet it was also shown in prior research that the higher metal loading led to more carbon monoxide being released during dehydrogenation because of the iron oxide that is formed.

CHAPTER 5. CONCLUSION

To keep up with hydrogen demand without contributing to global climate change, microwave-assisted thermocatalytic dehydrogenation of fossil fuels proposes a solution for hydrogen production with no CO_2 emissions. However, specified catalysts must be fabricated to meet the requirements of hydrogen yield and selectivity. The present research investigated two potential catalysts produced via solution combustion synthesis and incipient wetness impregnation. Based on each catalysts' characterization, iron-based alumina ($FeAl_xO_y$) catalysts produced through solution combustion synthesis are superior catalysts for dehydrogenation to iron-based (Fe/SiC) catalysts produced through incipient wetness impregnation. In terms of catalysis for 'green chemistry', high specific surface area is favorable because it allows more reactants to reach the molecules of the catalysts. Specific surface areas in solution combustion synthesis products were approximately 10x higher than those in incipient wetness impregnation products.

In addition, three parameters (fuel type, heat mode, and Fe/Al mole ratio) were varied in the production of iron-based alumina catalysts through solution combustion synthesis. Each parameter affected the product characteristics determined with X-ray diffraction analysis, scanning electron microscopy, laser diffraction particle size analysis, and BET surface area analysis – with some parameters more predominant than the others. Based upon the characterization results, it is suggested that using citric acid as the fuel and a muffle furnace as a heating mode will yield the best materials for dehydrogenation. From the varied Fe:Al mole ratios (1:2, 1:1, and 2:1), 1:2 produced the highest specific surface area; yet according to XRD results, this is an effect from the amorphous structure of aluminum oxide formed. Hence, 1:1 Fe/Al ratio is favored between the three tested, but further testing could approximate the superlative Fe/Al mole ratio in between 1:2 and 1:1.

REFERENCES

[1]   van Renssen, S. The hydrogen solution?. *Nat. Clim. Chang.* 10, 799–801 (2020). https://doi.org/10.1038/s41558-020-0891-0

[2]   Griffiths, S., Sovacool, B. K., Kim, J., Bazilian, M., & Uratani, J. M. (2021). Industrial decarbonization via hydrogen: A critical and systematic review of developments, socio-technical systems and Policy Options. *Energy Research & Social Science*, *80*, 102208. https://doi.org/10.1016/j.erss.2021.102208

[3]   Furat Dawood, Martin Anda, G.M. Shafiullah, Hydrogen production for energy: An overview, *International Journal of Hydrogen Energy*, Volume 45, Issue 7, 2020, Pages 3847-3869, ISSN 0360-3199, https://doi.org/10.1016/j.ijhydene.2019.12.059.

[4]   Birol, Fatih. "The future of hydrogen: seizing today's opportunities." *IEA Report prepared for the G* 20 (2019).

[5]   M. Hermesmann, T.E. Müller, Green, Turquoise, Blue, or Grey? Environmentally friendly Hydrogen Production in Transforming Energy Systems, *Progress in Energy and Combustion Science*, Volume 90, 2022, 100996, ISSN 0360-1285, https://doi.org/10.1016/j.pecs.2022.100996.

[6]   Newborough M, Cooley G. Developments in the global hydrogen market: The spectrum of hydrogen colours. *Fuel Cells Bulletin* 2020;2020 (11):16–22. https://doi.org/10.1016/S1464-2859(20)30546-0.

[7]   M. Hermesmann, K. Grübel, L. Scherotzki, T.E. Müller, Promising pathways: The geographic and energetic potential of power-to-x technologies based on regeneratively obtained hydrogen, *Renewable and Sustainable Energy Reviews*, Volume 138, 2021, 110644, ISSN 1364-0321, https://doi.org/10.1016/j.rser.2020.110644.

[8]   Horikoshi, S., & Serpone, N. (2014). Role of microwaves in heterogeneous catalytic systems. *Catalysis Science & Technology*, *4*(5), 1197. https://doi.org/10.1039/c3cy00753g

[9]   Jie, X., Chen, R., Biddle, T., Slocombe, D. R., Dilworth, J. R., Xiao, T., & Edwards, P. P. (2022). Size-dependent microwave heating and catalytic activity of fine iron particles in the deep dehydrogenation of hexadecane. *Chemistry of Materials*, *34*(10), 4682–4693. https://doi.org/10.1021/acs.chemmater.2c00630

[10]   Jie, X., Gonzalez-Cortes, S., Xiao, T., Yao, B., Wang, J., Slocombe, D. R., Fang, Y., Miller, N., Al-Megren, H. A., Dilworth, J. R., Thomas, J. M., & Edwards, P. P. (2019). The decarbonisation of petroleum and other fossil hydrocarbon fuels for the facile production and safe storage of hydrogen. *Energy & Environmental Science*, *12*(1), 238–249. https://doi.org/10.1039/c8ee02444h

[11]   Jie, X., Li, W., Slocombe, D., Gao, Y., Banerjee, I., Gonzalez-Cortes, S., Yao, B., AlMegren, H., Alshihri, S., Dilworth, J., Thomas, J., Xiao, T., & Edwards, P. (2020). Microwave-initiated catalytic deconstruction of plastic waste into hydrogen and high-value carbons. *Nature Catalysis*, *3*(11), 902–912. https://doi.org/10.1038/s41929-020-00518-5

[12]   Jie, X., Xiao, T., Yao, B., Gonzalez-Cortes, S., Wang, J., Fang, Y., Miller, N., AlMegren, H., Dilworth, J. R., & Edwards, P. P. (2018). On the performance optimisation of Fe catalysts in the microwave - assisted H2 production by the dehydrogenation of hexadecane. *Catalysis Today*, *317*, 29–35. https://doi.org/10.1016/j.cattod.2018.03.036

[13]   Jie, X., Gonzalez-Cortes, S., Xiao, T., Wang, J., Yao, B., Slocombe, D. R., Al-Megren, H. A., Dilworth, J. R., Thomas, J. M., & Edwards, P. P. (2017). Rapid production of high-purity hydrogen fuel through microwave-promoted deep catalytic dehydrogenation of liquid alkanes with abundant metals. *Angewandte Chemie*, *129*(34), 10304–10307. https://doi.org/10.1002/ange.201703489

[14]   Wilcox, J. (2014). Grand challenges in Advanced Fossil Fuel Technologies. *Frontiers in Energy Research*, *2*. https://doi.org/10.3389/fenrg.2014.00047

[15]   Guéret, C., Daroux, M., & Billaud, F. (1997). Methane pyrolysis: Thermodynamics. *Chemical Engineering Science*, *52*(5), 815–827. https://doi.org/10.1016/s0009-2509(96)00444-7

[16]   Varma, A., Mukasyan, A. S., Rogachev, A. S., & Manukyan, K. V. (2016). Solution combustion synthesis of nanoscale materials. *Chemical Reviews*, *116*(23), 14493–14586. https://doi.org/10.1021/acs.chemrev.6b00279

[17]   González-Cortés, S. L., & Imbert, F. E. (2013). Fundamentals, properties and applications of solid catalysts prepared by solution combustion synthesis (SCS). *Applied Catalysis A: General*, *452*, 117–131. https://doi.org/10.1016/j.apcata.2012.11.024

[18]   Specchia, S., Ercolino, G., Karimi, S., Italiano, C., & Vita, A. (2017). Solution combustion synthesis for preparation of structured catalysts: A mini-review on process intensification for energy applications and pollution control. *International Journal of Self-Propagating High-Temperature Synthesis*, *26*(3), 166–186. https://doi.org/10.3103/s1061386217030062

[19]   Pehlivan, M., Simsek, S., Ozbek, S., & Ozbek, B. (2019). An extensive study on the synthesis of iron based magnetic aluminium oxide nanocomposites by solution combustion method. *Journal of Materials Research and Technology*, *8*(2), 1746–1760. https://doi.org/10.1016/j.jmrt.2018.12.005

[20]   Novitskaya, E., Kelly, J. P., Bhaduri, S., & Graeve, O. A. (2020). A review of Solution Combustion Synthesis: An analysis of parameters controlling powder characteristics. *International Materials Reviews*, *66*(3), 188–214. https://doi.org/10.1080/09506608.2020.1765603

[21] Jadhav, L. D., Patil, S. P., Jamale, A. P., & Chavan, A. U. (2013). Solution combustion synthesis: Role of oxidant to fuel ratio on powder properties. *Materials Science Forum*, *757*, 85–98. https://doi.org/10.4028/www.scientific.net/msf.757.85

[22] Zavyalova, U., Scholz, P., & Ondruschka, B. (2007). Influence of Cobalt Precursor and fuels on the performance of combustion synthesized co3o4/γ-al2o3 catalysts for total oxidation of methane. *Applied Catalysis A: General*, *323*, 226–233. https://doi.org/10.1016/j.apcata.2007.02.021

[23] Jain, S. R., Adiga, K. C., & Pai Verneker, V. R. (1981). A new approach to thermochemical calculations of condensed fuel-oxidizer mixtures. *Combustion and Flame*, *40*, 71–79. https://doi.org/10.1016/0010-2180(81)90111-5

[24] Naik, M. A., Mishra, B. G., & Dubey, A. (2008). Combustion synthesized wo3–zro2 nanocomposites as catalyst for the solvent-free synthesis of coumarins. *Colloids and Surfaces A: Physicochemical and Engineering Aspects*, *317*(1-3), 234–238. https://doi.org/10.1016/j.colsurfa.2007.10.019

[25] Xanthopoulou, G., Thoda, O., Metaxa, E. D., Vekinis, G., & Chroneos, A. (2017). Influence of atomic structure on the nano-nickel-based catalyst activity produced by solution combustion synthesis in the hydrogenation of maleic acid. *Journal of Catalysis*, *348*, 9–21. https://doi.org/10.1016/j.jcat.2016.12.002

[26] Toniolo, J. C., Takimi, A. S., & Bergmann, C. P. (2010). Nanostructured Cobalt Oxides (co3o4 and COO) and metallic co powders synthesized by the solution combustion method. *Materials Research Bulletin*, *45*(6), 672–676. https://doi.org/10.1016/j.materresbull.2010.03.001

[27] H. Aliasghari, A.M. Arabi, H. Haratizadeh, A novel approach for solution combustion synthesis of tungsten oxide nanoparticles for photocatalytic and electrochromic applications, *Ceramics International*, Volume 46, Issue 1, 2020, Pages 403-414, ISSN 0272-8842, https://doi.org/10.1016/j.ceramint.2019.08.275.

[28] Carlos, E., Martins, R., Fortunato, E., & Branquinho, R. (2020). Solution combustion synthesis: Towards a sustainable approach for metal oxides. *Chemistry – A European Journal*, *26*(42), 9099–9125. https://doi.org/10.1002/chem.202000678

[29] Salem, S. (2015). Rapid combustion synthesis of pure nano-crystalline gahnite: Effect of solution ph on powder characteristics. *Thermochimica Acta*, *609*, 75–81. https://doi.org/10.1016/j.tca.2015.04.017

[30] Goldstein, J. (2003). *Scanning Electron Microscopy and X-Ray Microanalysis*. Springer. https://books.google.com/books?id=ruF9DQxCDLQC

VITA

Victoria Isabel Reyes was born and raised in El Paso, Texas. She enrolled at the University of Texas at El Paso part-time in August 2015 during her senior year of high school through the early college program at Mission Early College High School. After graduating valedictorian from high school in May 2016, she continued her studies full-time at UTEP. She received her Bachelor of Science in Mechanical Engineering degree in December 2019. After being accepted into the UTEP graduate program for Mechanical Engineering, she continued her education in January 2021. Since summer 2021, she conducted research under the supervision of Dr. Shafirovich in the Aerospace Center at UTEP. She prepared combustible liquid mixtures along with characterizing the products that would be used for the dehydrogenation of fossil fuels. The results of her research were presented at the 2022 Spring Technical Meeting of the Central States Section of The Combustion Institute, May 15-17, 2022, Detroit, MI, and at the 2022 Annual Meeting of the American Institute of Chemical Engineers (AIChE), November 13-18, 2022, Phoenix, AZ. In summer 2022, she conducted research at McGill University (Montreal, Canada) on the combustion of metals as clean energy carriers.

Contact information: Victoria Isabel Reyes

University email: vireyes@miners.utep.edu